materials

MDPI

Article

Energy Transfer Study on Tb^{3+}/Eu^{3+} Co-Activated Sol-Gel Glass-Ceramic Materials Containing MF_3 (M = Y, La) Nanocrystals for NUV Optoelectronic Devices

Natalia Pawlik *, Barbara Szpikowska-Sroka and Wojciech A. Pisarski *

Institute of Chemistry, University of Silesia, 40-007 Katowice, Poland; barbara.szpikowska-sroka@us.edu.pl

* Correspondence: natalia.pawlik@us.edu.pl (N.P.); wojciech.pisarski@us.edu.pl (W.A.P.)

Received: 22 April 2020; Accepted: 28 May 2020; Published: 1 June 2020

Abstract: In the present work, the Tb^{3+}/Eu^{3+} co-activated sol-gel glass-ceramic materials (GCs) containing MF_3 (M = Y, La) nanocrystals were fabricated during controlled heat-treatment of silicate xerogels at 350 °C. The studies of $Tb^{3+} \rightarrow Eu^{3+}$ energy transfer process (ET) were performed by excitation and emission spectra along with luminescence decay analysis. The co-activated xerogels and GCs exhibit multicolor emission originated from $4f^n$–$4f^n$ optical transitions of Tb^{3+} ($^5D_4 \rightarrow {}^7F_J$, J = 6–3) as well as Eu^{3+} ions ($^5D_0 \rightarrow {}^7F_J$, J = 0–4). Based on recorded decay curves, it was found that there is a significant prolongation in luminescence lifetimes of the $^5D_4$ (Tb^{3+}) and the $^5D_0$ (Eu^{3+}) levels after the controlled heat-treatment of xerogels. Moreover, for both types of prepared GCs, an increase in ET efficiency was also observed (from $\eta_{ET} \approx 16\%$ for xerogels up to $\eta_{ET} = 37.3\%$ for SiO_2-YF_3 GCs and $\eta_{ET} = 60.8\%$ for SiO_2-LaF_3 GCs). The changes in photoluminescence behavior of rare-earth (RE^{3+}) dopants clearly evidenced their partial segregation inside low-phonon energy fluoride environment. The obtained results suggest that prepared SiO_2-MF_3:Tb^{3+}, Eu^{3+} GC materials could be considered for use as optical elements in RGB-lighting optoelectronic devices operating under near-ultraviolet (NUV) excitation.

Keywords: Tb^{3+}/Eu^{3+} energy transfer; sol-gel technique; glass-ceramics; NUV excitation

1. Introduction

The development of materials dedicated to photonic applications is a frontier area of current materials engineering research [1,2]. Thus, considerable efforts are still being made to improve the optical parameters of such materials, e.g., the tuning of emissions in the desired spectrum range. In this case, the willingly studied pathway for generation a white light is related to the mixing of three primary colors—red, green and blue (RGB)—in optical materials. Such red-green-blue multicolor visible light can be achieved via up-conversion of near-infrared radiation (NIR) [3–7] or via the conversion of near-ultraviolet (NUV) photons [8–10]. Since rare-earth ions (RE^{3+}) exhibit a broad range of emission in the visible (VIS) spectral scope via interactions with NIR and NUV irradiation, they are considered as essential parts in the development of white-light-emitting RGB materials [11,12]. The first of abovementioned ways of generating RGB emission can be realized via NIR up-conversion excitation in doubly (e.g., Yb^{3+}/Er^{3+} [3,4], Yb^{3+}/Tm^{3+} [4]) and triply doped (e.g., $Yb^{3+}/Er^{3+}/Tm^{3+}$ [5,6], $Tb^{3+}/Tm^{3+}/Yb^{3+}$ [7]) optical systems. For example, for $Yb^{3+}/Er^{3+}/Tm^{3+}$ triply doped β-$NaYF_4$ microrods, Er^{3+} ions are responsible for the generation of red (the $^4F_{9/2} \rightarrow {}^4I_{15/2}$ transition) as well as green (the $^2H_{11/2} \rightarrow {}^4I_{15/2}$ and the $^4S_{3/2} \rightarrow {}^4I_{15/2}$ transitions) emissions through a two-photon absorption process involved in $Yb^{3+} \rightarrow Er^{3+}$ energy transfer. Simultaneously, due to the three-photon assisted process of $Yb^{3+} \rightarrow Tm^{3+}$ energy transfer, Tm^{3+} ions are able to emit blue

light (the $^1D_2 \rightarrow {}^3F_4$ and the $^1G_4 \rightarrow {}^3H_6$ transitions) [5]. The second of the abovementioned routes can be realized via the successful conversion of NUV irradiation into VIS light. In this matter, Eu^{3+} ions are treated as a red or reddish-orange light source (the $^5D_0 \rightarrow {}^7F_J$ transitions, J = 0–4) and Tb^{3+} ions are considered as one of the most important sources of green emission (the $^5D_4 \rightarrow {}^7F_5$ transition). Therefore, co-doping with Tb^{3+}/Eu^{3+} ions seems to be a promising strategy for the generation of multicolor luminescence, which plays a key role in RGB optical materials [13–16].

Another particularly important point in the field of substantial enhancement, the luminescence of RE^{3+} ions is related to the selection of a suitable host lattice with low phonon energy. Since the phonon energies of fluorides—usually in a range from 400 up to 500 cm^{-1} [17]—are significantly lower compared to phosphates (~1250 cm^{-1}) [18] or borates (~1350 cm^{-1}) [19], they are considered as great candidates for generating an efficient and long-lived luminescence of RE^{3+}. Among fluorides, special attention should be paid to YF_3 and LaF_3 crystal phases characterized by wide band gap (>10 eV) and exceptionally low-phonon energies equal to ~358 as well as ~350 cm^{-1}, respectively, in which M^{3+} (M = Y, La) cations from crystal lattices can be easily substituted by RE^{3+} ions without any charge compensation [20–23]. Due to the above reasons, the oxyfluoride glass-ceramic materials (GCs) containing fluoride nanocrystals are considered as an interesting class of advanced optical materials, which are frequently reported in the literature [24–28]. Indeed, they successfully combine the advantages of the individual fluoride crystal phase with good mechanical strength and thermal durability of oxide hosts [29,30]. It should also be noted that due to the compliance with the principles of green chemistry, the systematic elimination of PbF_2 (characterized by exceptionally low-phonon energy equals to ~250 cm^{-1} [31]) during preparation is currently a very important aspect. Thus, taking the above considerations into account, Tb^{3+}/Eu^{3+} co-doped oxyfluoride GCs containing selected fluoride phases (e.g., YF_3 and LaF_3) seems to be a good choice for the generation of efficient visible emissions.

The conventional melt-quenching method followed by controlled heat-treatment at specified time and temperature conditions is currently the most widely used technique for fabricating the class of oxyfluoride GCs [32–36]. On the other hand, the high melting temperatures of glass-forming components (e.g., 1450 °C, 1500 °C [37–39]) increase the risk of volatilization of the fluoride compounds, which may adversely affect the crystallization process of the fluoride fraction. Therefore, an alternative route to obtain oxyfluoride GCs is the sol-gel technique, characterized by low-temperature processing [40–42]. This method is based on hydrolysis, condensation and polycondensation reactions of organometallic precursors, usually alkoxysilanes $Si(OR)_4$ (R = $–CH_3$, $–C_2H_5$, etc.) in a liquid phase at room temperature [43]. The in-situ crystallization of fluoride phases is possible due to introduction of a fluorinating reagent into reaction system at initial stages, whose role is commonly played by trifluoroacetic acid (TFA) [44]. Since the sintering of sol-gel materials is carried out at significantly lower temperatures (usually <500 °C) than the conventional melt-quenching of glasses, a risk of volatilization of fluorides is adequately lower, meaning that sol-gel processing is preferred. Lower energy consumption also makes the sol-gel technique particularly advantageous and attractive from an environmental friendliness point of view. Simultaneously, to the best of our knowledge, the investigation of Tb^{3+}/Eu^{3+} energy transfer process in oxyfluoride GCs is extremely rarely described in the available literature. In the literature, there is only one excellent description concentrated on YF_3:Tb^{3+}, Eu^{3+} nanocrystalline-based GCs fabricated from $44SiO_2$-$28Al_2O_3$-17NaF-(10 – x)YF_3-$TbF_{3-x}EuF_3$ (x = 0, 0.1, 0.25, 1) glasses during their heat-treatment at 670 °C per 2 h, as far as we know [45]. Due to the above reasons, it seems to be justified to study the $Tb^{3+} \rightarrow Eu^{3+}$ energy transfer in sol-gel GCs containing MF_3 (M = La or Y) nanocrystals.

In the present work, the sol-gel oxyfluoride GCs materials containing MF_3:Tb^{3+}, Eu^{3+} (M = Y, La) nanocrystals were successfully fabricated during controlled heat-treatment at low temperature (350 °C per 10 h) and characterized by detailed luminescence measurements. The studies were performed by means of excitation and emission spectra along with lifetime measurements. Based on photoluminescence results, the interactions between Tb^{3+} and Eu^{3+} dopant ions were systematically investigated and the incorporation of dopant ions into the fluoride environment was also analyzed.

2. Materials and Methods

The xerogels co-doped with Tb^{3+} and Eu^{3+} ions were synthesized using the low-temperature sol-gel method. All reagents used during the described procedure were taken from Aldrich Chemical Co. The sol-gel synthesis was started with the introduction of tetraethoxysilane (TEOS, 98%), ethyl alcohol (98%), deionized water (from Elix 3 system, Millipore, Molsheim, France) and acetic acid (99.5–99.9%) into round-bottom flasks. The molar ratio of components was equal to TEOS:C_2H_5OH:H_2O:CH_3COOH = 1:4:10:0.5 (90 wt.%). To perform hydrolysis and to initialize a condensation reaction, the components were stirred for 30 min. During the next step, the appropriate amounts of acetates, i.e., $M(CH_3COO)_3$ (M = Y, La; 99.9%) as well as $Tb(CH_3COO)_3$ (99.999%) and $Eu(CH_3COO)_3$ (99.999%) were weighed and dissolved in trifluoroacetic acid (TFA, 99%) and obtained mixtures were added into TEOS-based solutions. The molar ratio was equal to CF_3COOH:$M(CH_3COO)_3$:$Tb(CH_3COO)_3$:$Eu(CH_3COO)_3$ = 5:1:0.05:0.05 (10 wt.%) (M = Y, La). The resultant solutions were mixed for another 60 min. After sol-gel synthesis, the obtained liquid sols were dried at 35 °C for 7 weeks to form colorless and transparent solid xerogels (denoted in the text as XGs). Their further transformation into glass-ceramic materials containing YF_3 and LaF_3 nanocrystals was realized by controlled heat-treatment in a muffle furnace (FCF 5 5SHP produced by Czylok, Jastrzębie-Zdrój, Poland) at 350 °C per 10 h (the temperature was raised by 10 °C/min from room temperature). After this procedure, the samples were slowly cooled down to room temperature (denoted in the text as SiO_2-MF_3, M = Y, La). The successful formation of fluoride nanocrystals (LaF_3 NCs: *P6₃/mmc*, ICDD PDF-2 No. 08-0461; YF_3 NCs: *Pnma*, ICDD PDF-2 No. 32-1431) was verified using X-ray diffraction (XRD, X'Pert Pro diffractometer, Panalytical, Almelo, The Netherlands) and the nanocrystals imaging was done via high-resolution transmission electron microscope (HR-TEM, JEOL JEM 3010, Tokyo, Japan). The results are shown in Figure 1. The average diameters of fabricated nanocrystals were estimated to 8.1 nm for LaF_3 and 15.4 nm for YF_3. The in-situ formation of LaF_3 and YF_3 nanocrystals during the thermal decomposition of $La(CF_3COO)_3$ as well as $Y(CF_3COO)_3$ in applied heat-treatment conditions (350 °C, 10 h) was confirmed and reported in details in our previous works [46,47].

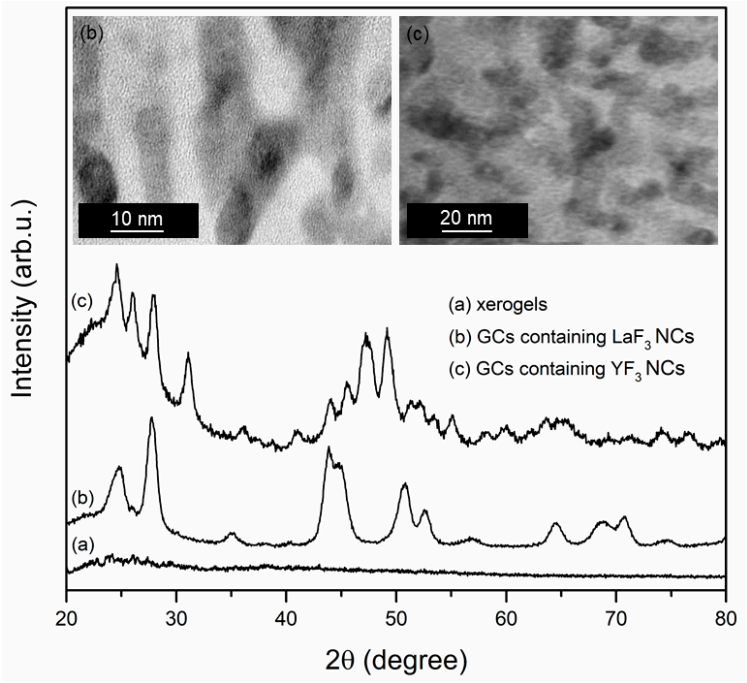

Figure 1. Transmission electron microscope (TEM) images and X-ray diffraction (XRD) patterns of fabricated xerogels and glass-ceramic samples.

The excitation and emission spectra as well as decay curves were recorded on Horiba Jobin Yvon FluoroMax-4 spectrofluorimeter (Horiba Jobin Yvon, Longjumeau, France) supplied with 150 W Xe

lamp. The spectra were recorded with ± 0.1 nm resolution and the decay curves were recorded with ± 2 μs accuracy. All structural and luminescence measurements were carried out at room temperature.

3. Results and Discussion

3.1. Excitation Spectra of Fabricated Tb^{3+},Eu^{3+} Co-Doped Sol-Gel Materials

Figures 2 and 3 present the photoluminescence excitation (PLE) spectra of fabricated Tb^{3+}/Eu^{3+} co-doped xerogels. The PLE spectra were recorded in the spectral range from 340 to 520 nm and monitored at λ_{em} = 543 nm and λ_{em} = 612 nm emissions (the $^5D_4 \rightarrow {}^7F_5$ green line of Tb^{3+} ions and the $^5D_0 \rightarrow {}^7F_2$ red line of Eu^{3+}, respectively). The recorded bands were attributed to the $4f^8$–$4f^8$ and $4f^6$–$4f^6$ intra-configurational transitions from both of optically active ions. The bands originating from Eu^{3+} were assigned to the following transitions: $^7F_0 \rightarrow {}^5D_4$ (363 nm), $^7F_0 \rightarrow {}^5G_J$, $^5L_7$ (from 372 nm to 389 nm), $^7F_0 \rightarrow {}^5L_6$ (394 nm) and $^7F_0 \rightarrow {}^5D_2$ (464 nm). Among the group of excitation bands originated from Tb^{3+} ions, the transitions were ascribed to the electronic transitions from the $^7F_6$ ground level into the subsequent upper-lying states: $^5L_9$ (352 nm), $^5L_{10}$ (370 nm), $^5D_3$ (378 nm) and $^5D_4$ (488 nm).

The selection of excitation parameters for further emission measurements and to study the $Tb^{3+} \rightarrow Eu^{3+}$ energy transfer process was done from the near-UV (NUV) irradiation area (<400 nm) due to the greater intensity of recorded excitation lines than in visible light (VIS) scope (>400 nm). Indeed, the optical elements considered to be used in RGB-lighting devices should operate under NUV excitation. Since the $^7F_0 \rightarrow {}^5L_6$ excitation band of Eu^{3+} is the most intense, we decided to perform the luminescence measurements for Eu^{3+} ions using λ_{exc} = 394 nm wavelength.

As the band associated to the $^7F_6 \rightarrow {}^5L_9$ transition of Tb^{3+} ions does not coincide with any excitation peak of Eu^{3+}, the choice of λ_{exc} = 352 nm wavelength as the excitation source for the generation of the $Tb^{3+} \rightarrow Eu^{3+}$ energy transfer seems to be reasonable. Additionally, in order to compare the luminescence behavior of sol-gel samples co-doped with Tb^{3+}/Eu^{3+} ions with samples singly doped with Tb^{3+} ions, all photoluminescence measurements for Tb^{3+} ions were performed using the λ_{exc} = 352 nm excitation line.

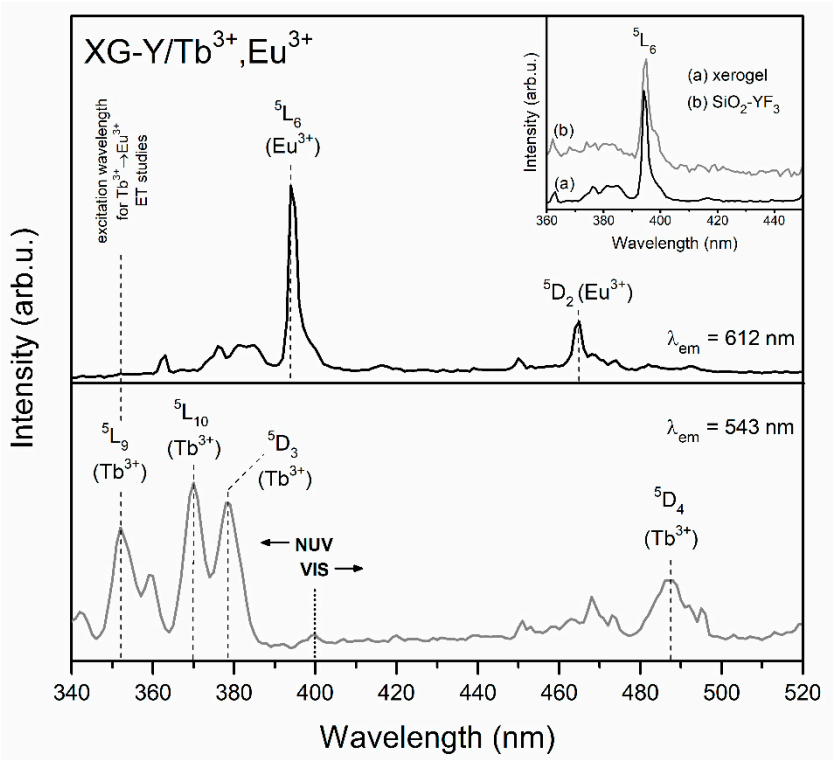

Figure 2. Photoluminescence excitation (PLE) spectra of XG-Y/Tb^{3+},Eu^{3+} co-doped sample, monitored at λ_{em} = 543 nm and λ_{em} = 612 nm.

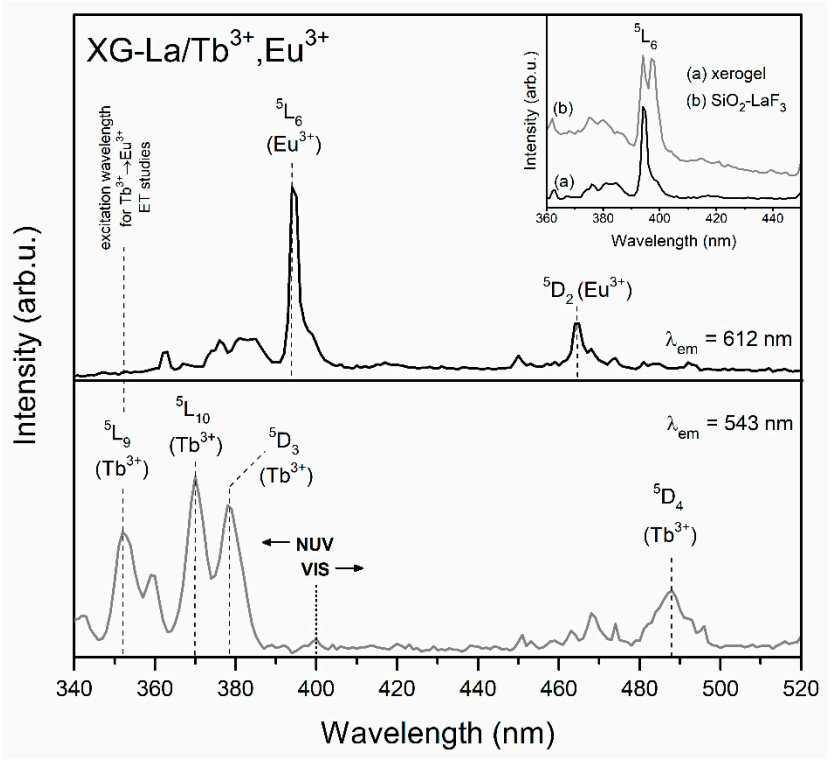

Figure 3. PLE spectra of XG-La/Tb^{3+},Eu^{3+} co-doped sample, monitored at λ_{em} = 543 nm and λ_{em} = 612 nm.

It should be also noted that for prepared GC samples, the $^7F_0 \rightarrow {}^5L_6$ excitation line was split into two separated components, the maxima of which were located at 394 and 397 nm (shown in inset of Figures 2 and 3). Similar results were reported by A.C. Yanes et al. [48] for sol-gel glass-ceramics with 89.9SiO_2-10LaF_3:0.1EuF_3 (mol %) composition. Based on numerous photoluminescence measurements (excitation and emission spectra recorded at different temperatures: room temperature (RT), 100 and 13 K; analysis of emission spectra under excitation at 393 and 396 nm), it was clearly proven that the two PLE components are strictly related to the distribution of Eu^{3+} between the SiO_2 sol-gel host (393 nm component) and LaF_3 nanocrystals (396 nm component). Thus, in the case of our studied sol-gel samples, we also assumed that the origin of such a split after the controlled heat-treatment of xerogels (XG-Y/Tb^{3+},Eu^{3+} and XG-La/Tb^{3+},Eu^{3+}) is related to the partial migration of rare-earths from silicate sol-gel host into MF_3 (M = Y, La) nanocrystals. It is quite interesting that deeper splitting of the $^7F_0 \rightarrow {}^5L_6$ band was observed for SiO_2-LaF_3:Tb^{3+},Eu^{3+} GC and, in consequence, two strong components with maxima at 394 and 397 nm are visible. For the SiO_2-YF_3:Tb^{3+},Eu^{3+} GC sample, the 397 nm component is visible as a weak shoulder. This effect may suggest more efficient segregation of dopant ions in LaF_3 than YF_3 nanocrystals. Analogous results were reported earlier by us for singly doped SiO_2-YF_3:Eu^{3+} [46] and SiO_2-LaF_3:Eu^{3+} [47] GC sol-gel systems.

3.2. Influence of Controlled Heat-Treatment at 350 °C on $Tb^{3+} \rightarrow Eu^{3+}$ Energy Transfer

The photoluminescence (PL) spectra recorded for prepared silicate xerogels are illustrated in Figure 4 (XG-Y/Tb^{3+} and XG-Y/Tb^{3+},Eu^{3+}) as well as in Figure 5 (XG-La/Tb^{3+} and XG-La/Tb^{3+},Eu^{3+}). The excitation of Eu^{3+} ions using the λ_{exc} = 394 nm wavelength resulted in the appearance of luminescence bands located within the reddish-orange light area: $^5D_0 \rightarrow {}^7F_0$ (578 nm), $^5D_0 \rightarrow {}^7F_1$ (592 nm), $^5D_0 \rightarrow {}^7F_2$ (611 nm), $^5D_0 \rightarrow {}^7F_3$ (645 nm), and $^5D_0 \rightarrow {}^7F_4$ (698 nm). Since the local framework around Eu^{3+} ions in sol-gel host is non-symmetric, the most intense emission line corresponds to the $^5D_0 \rightarrow {}^7F_2$ electric-dipole transition and red-to-orange ratio (R/O) values for fabricated xerogels are relatively high (R/O = 3.01 for XG-Y/Tb^{3+},Eu^{3+}; R/O = 2.78 for XG-La/Tb^{3+},Eu^{3+}).

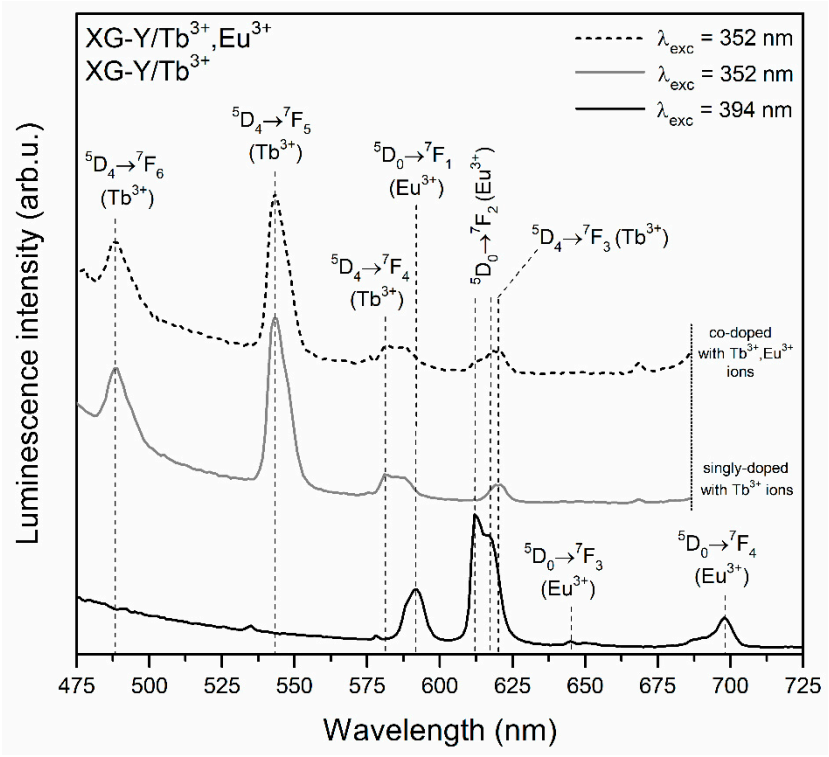

Figure 4. Photoluminescence (PL) spectra of XG-Y/Tb^{3+} and XG-Y/Tb^{3+},Eu^{3+} samples recorded upon near-ultraviolet (NUV) illumination at λ_{exc} = 352 nm and λ_{exc} = 394 nm.

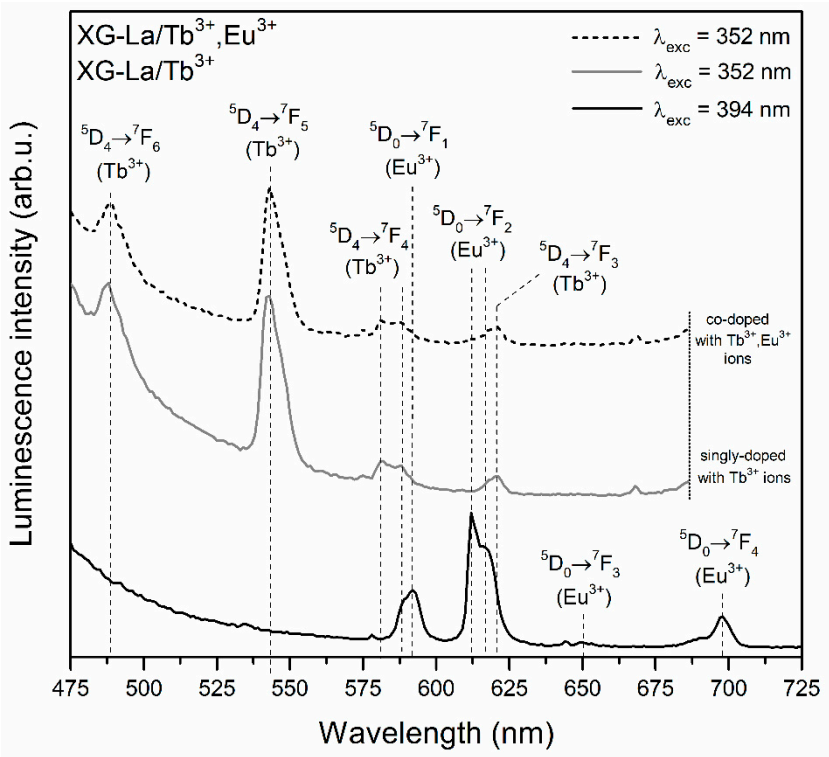

Figure 5. PL spectra of XG-La/Tb^{3+} and XG-La/Tb^{3+},Eu^{3+} samples recorded upon NUV illumination at λ_{exc} = 352 nm and λ_{exc} = 394 nm.

The PL spectra recorded upon excitation at λ_{exc} = 352 nm for xerogels singly doped with Tb^{3+} ions revealed two emission bands in the bluish-green spectral scope, i.e., $^5D_4 \rightarrow {}^7F_6$ (488 nm) and the most prominent $^5D_4 \rightarrow {}^7F_5$ (543 nm) line. Two another emission bands of Tb^{3+} ions were detected in

the yellowish-red range: $^5D_4 \rightarrow {}^7F_4$ (584 nm) and $^5D_4 \rightarrow {}^7F_3$ (619 nm). The excitation of Tb^{3+}/Eu^{3+} co-doped xerogels using λ_{exc} = 352 nm wavelength led to generating the characteristic emission lines of Tb^{3+} ions; however, it should be noted that some spectral broadening of the $^5D_4 \rightarrow {}^7F_4$ as well as the $^5D_4 \rightarrow {}^7F_3$ bands was observed. Such broadening is a consequence of the energy transfer process from Tb^{3+} to Eu^{3+}, which resulted in the appearance of additional luminescence coming from Eu^{3+} dopant ($^5D_0 \rightarrow {}^7F_1$ and $^5D_0 \rightarrow {}^7F_2$ transitions) [49–52]. In general, the spectral matching of donor's emission (Tb^{3+}) and acceptor's excitation (Eu^{3+}) regions is a fundamental condition for energy transfer occurrence. In this way, upon irradiation using λ_{exc} = 352 nm line from NUV spectral region, Tb^{3+} ions could be successfully pumped into the $^5L_9$ level and then the non-radiative de-activation to the $^5D_4$ state takes place. Since there is spectral overlapping between the $^5D_4 \rightarrow {}^7F_5$,$^7F_4$ emissions of $Tb^{3+}$and the $^7F_1 \rightarrow {}^5D_1$ and the $^7F_0$, $^7F_1 \rightarrow {}^5D_0$ excitation bands of Eu^{3+}, the energy could be successfully transferred from Tb^{3+} into Eu^{3+} ions as follows [53,54]:

$^5D_4$ (Tb^{3+}) + $^7F_1$ (Eu^{3+}) $\rightarrow {}^7F_5$ (Tb^{3+}) + $^5D_1$ (Eu^{3+}) (1),

$^5D_4$ (Tb^{3+}) + ($^7F_0$, $^7F_1$) (Eu^{3+}) $\rightarrow {}^7F_4$ (Tb^{3+}) + $^5D_0$ (Eu^{3+}) (2).

Hence, among the characteristic emission lines from Tb^{3+} ions, additional bands originated from Eu^{3+} can also be recorded. The matching of Tb^{3+} emission and Eu^{3+} excitation as well as illustration of energy levels involved in $Tb^{3+} \rightarrow Eu^{3+}$ energy transfer process are depicted in Figure 6.

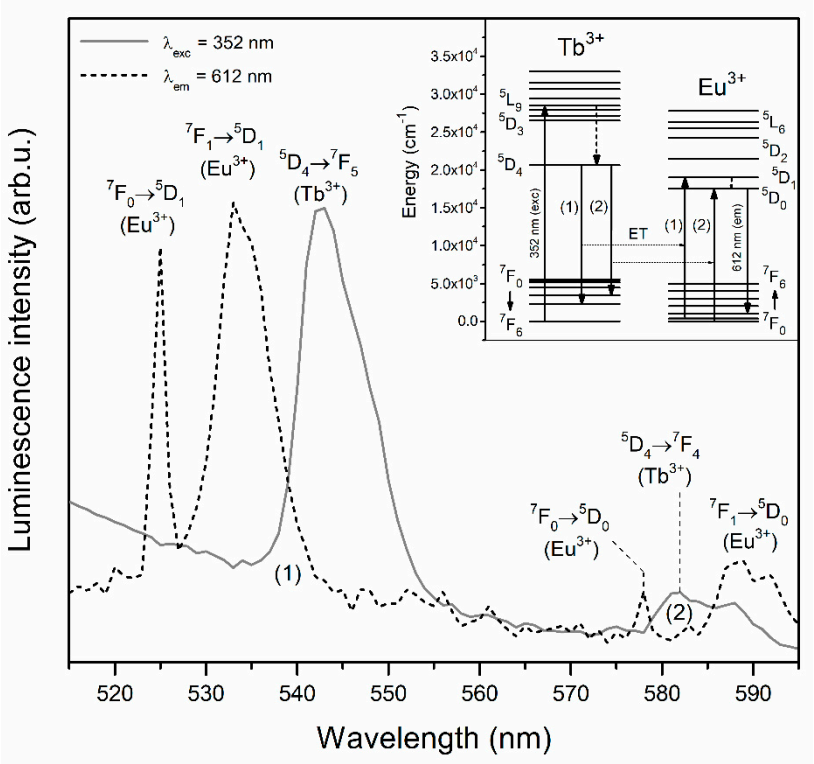

Figure 6. An overlap of Tb^{3+} emission (λ_{exc} = 352 nm) and Eu^{3+} excitation (λ_{em} = 612 nm) regions and illustration of energy levels involved in $Tb^{3+} \rightarrow Eu^{3+}$ energy transfer process.

The PL spectra recorded for glass-ceramic materials are shown in Figure 7 (SiO_2-YF_3:Tb^{3+} and SiO_2-YF_3:Tb^{3+},Eu^{3+}) and Figure 8 (SiO_2-LaF_3:Tb^{3+} and SiO_2-LaF_3:Tb^{3+},Eu^{3+}). For both types of prepared co-doped GC, a well-resolved Stark structure of recorded luminescence bands of Eu^{3+} ions was observed, which points to crystalline-like environment around them. For SiO_2-YF_3:Tb^{3+}, Eu^{3+} GCs the following maxima are located at: 586/592/594 nm ($^5D_0 \rightarrow {}^7F_1$), 614 nm/619 nm ($^5D_0 \rightarrow {}^7F_2$), 650 nm ($^5D_0 \rightarrow {}^7F_3$) and 690/692/698 nm ($^5D_0 \rightarrow {}^7F_4$), while for SiO_2-YF_3:Tb^{3+}, Eu^{3+} GCs, the maxima of individual emission bands were detected at the following wavelengths: 590 nm ($^5D_0 \rightarrow {}^7F_1$), 612 nm/618 nm ($^5D_0 \rightarrow {}^7F_2$), 649 nm ($^5D_0 \rightarrow {}^7F_3$) and 680/688/692 nm ($^5D_0 \rightarrow {}^7F_4$). Such clear splitting is

a consequence of the partial segregation of Eu^{3+} ions inside fluoride crystal lattices. Indeed, when Eu^{3+} ions are inserted into the crystal lattice, the subsequent energy levels get split by the crystal-field effect and the number of sub-levels depends on the local site symmetry. It is reported in the literature that in YF_3 and LaF_3 crystal lattices, Eu^{3+} ions occupy C_s and C_{2v} point symmetry sites, respectively [55,56]. If Eu^{3+} ions occupy C_s and C_{2v} site symmetry, the J term of the ^7F_J levels should split into three (J = 1), five (J = 2), seven (J = 3) and nine (J = 4) sub-levels [57]. However, observation of such strong splitting for glass-ceramic systems is quite difficult due to the partial distribution of Eu^{3+} ions within the amorphous sol-gel host. Moreover, compared to xerogels, a significant increase in intensity of the $^5D_0 \rightarrow {}^7F_1$ magnetic-dipole transition band was observed, while the intensity of the $^5D_0 \rightarrow {}^7F_2$ electric-dipole transition is strongly inhibited. Generally, the $^5D_0 \rightarrow {}^7F_1$ magnetic-dipole transition is orbitally allowed and practically insensitive to symmetry in the local environment around Eu^{3+} ions. Conversely, the $^5D_0 \rightarrow {}^7F_{0,2-4}$ electric-dipole transitions are forbidden in centrosymmetric sites due to the same parity of energy levels. However, if Eu^{3+} ions are located in non-centrosymmetric sites, the transitions became allowed as forced electric-dipole transitions due to the mixing of wavefunctions of $4f^6$ sublevels with different J values. Therefore, the ratio of integrated luminescence intensity of the $^5D_0 \rightarrow {}^7F_2$ electric-dipole transition to the $^5D_0 \rightarrow {}^7F_1$ magnetic-dipole transition can inform us about local symmetry around Eu^{3+} ions and is called the R/O ratio. A decrease in R/O-ratio value clearly suggests that local symmetry around Eu^{3+} ions is closer to an inversion center. The calculated R/O ratio values after controlled heat-treatment are relatively low (R/O = 0.42 for SiO_2-YF_3:Tb^{3+},Eu^{3+}; R/O = 0.89 for SiO_2-LaF_3:Tb^{3+},Eu^{3+}), which clearly points to the partial migration of Eu^{3+} ions from sol-gel host into more symmetric fluoride crystal phases.

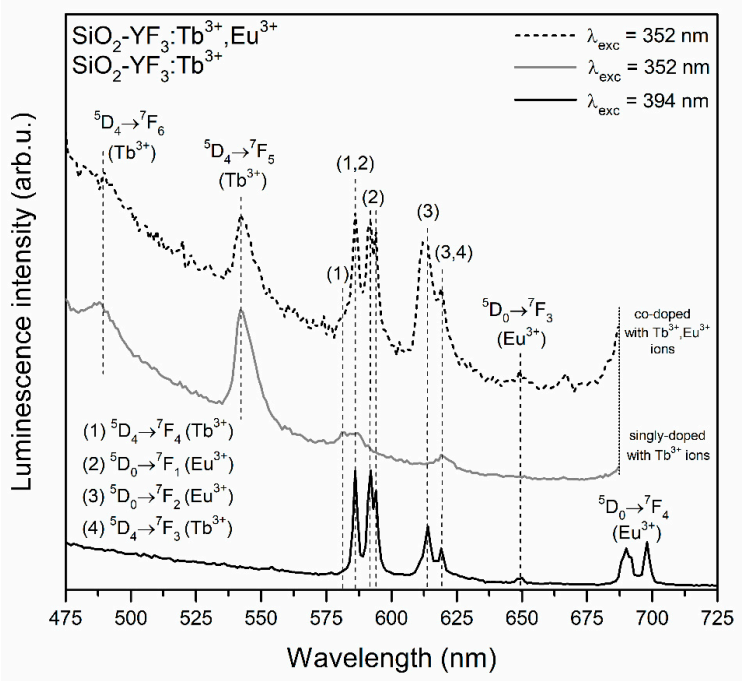

Figure 7. PL spectra of SiO_2-YF_3:Tb^{3+} and SiO_2-YF_3:Tb^{3+},Eu^{3+} samples recorded under NUV excitation at λ_{exc} = 352 nm and λ_{exc} = 394 nm.

For the prepared SiO_2-MF_3:Tb^{3+} GC samples, the characteristic emission bands corresponding to the transitions from the $^5D_4$ excited level into the $^7F_6$, $^7F_5$, $^7F_4$ and $^7F_3$ lower-lying states were detected. In the case of SiO_2-MF_3:Tb^{3+},Eu^{3+} co-doped GCs, the mutual coincidence of the luminescence lines originating from both of the rare-earths was clearly observed after excitation at the λ_{exc} = 352 nm line. Therefore, an appearance of characteristic emission bands coming from Eu^{3+} ions upon excitation of Tb^{3+} confirms the occurrence of $Tb^{3+} \rightarrow Eu^{3+}$ energy transfer.

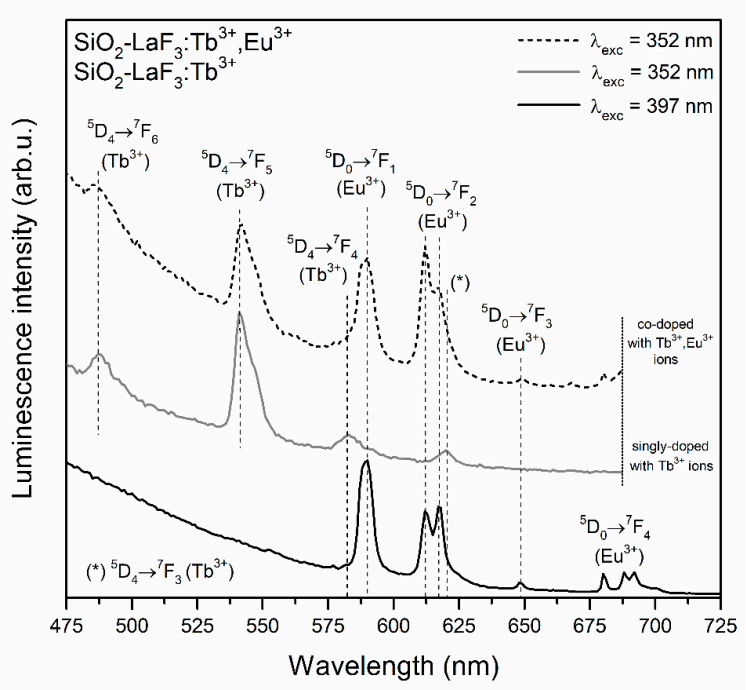

Figure 8. PL spectra of SiO_2-LaF_3:Tb^{3+} and SiO_2-LaF_3:Tb^{3+}, Eu^{3+} samples recorded under NUV excitation at λ_{exc} = 352 nm and λ_{exc} = 397 nm.

It should be particularly pointed out that the intensity of Tb^{3+} emission bands decreased, which was accompanied by the simultaneous enhancement of Eu^{3+} luminescence. Such an effect is much more observable for GC samples than for precursor xerogels. Hence, it could suggest that both of the optically active dopants were incorporated into the crystal lattices of the YF_3 as well as LaF_3 phases, causing there to be a shorter distance between neighboring Tb^{3+}-Eu^{3+} pairs in comparison with the sol-gel host. Thus, the $Tb^{3+} \rightarrow Eu^{3+}$ seems to be more efficient in glass-ceramic materials, which results in a much more intense emission of Eu^{3+} ions.

3.3. Luminescence Decay Analysis of the $^5D_4$ (Tb^{3+}) and the $^5D_0$ (Eu^{3+}) Levels in Sol-Gel Materials

To further optical examination of prepared xerogels and GC materials, the luminescence decay analysis of the $^5D_4$ (Tb^{3+}) and the $^5D_0$ (Eu^{3+}) excited states was performed. The analysis of decay profiles allows for the deeper characterization of the $Tb^{3+} \rightarrow Eu^{3+}$ energy transfer process and for establishing the relation between luminescence lifetimes and distribution of rare-earths within sol-gel materials.

Firstly, we compared the luminescence lifetimes of the $^5D_4$ level of Tb^{3+} ions in singly doped sol-gel materials (Figure 9) and materials co-doped with Tb^{3+}/Eu^{3+} ions (Figure 10). The decay curves were recorded upon NUV excitation (λ_{exc} = 352 nm) and monitoring a green emission related to the $^5D_4 \rightarrow {}^7F_5$ transition of Tb^{3+} (λ_{em} = 543 nm). For xerogels, the curves are well-fitted to mono-exponential functions given by:

$$I(t)/I_0 = A \times \exp(-t/\tau), \quad (1)$$

where τ corresponds to the luminescence decay time. It was observed that the τ ($^5D_4$) estimated for XG-Y/Tb^{3+} and XG-La/Tb^{3+} is quite comparable and equals 0.97 ± 0.01 and 0.89 ± 0.02 ms, respectively. Such negligible differences in luminescence lifetime values are caused by considerable similarity of chemical environment around Tb^{3+} in fabricated silicate xerogels. Indeed, the non-radiative relaxation between subsequent J states might occur due to the interaction of electronic levels of RE^{3+} ions with suitable vibrational modes in their nearest surrounding. As was proven earlier by infrared measurements, some liquids (residual solvents used during sol-gel process and products of homo-

and heterocondensation reactions) are retained in xerogel pores [46]. In this way, Tb^{3+} and Eu^{3+} ions are coordinated by CF_3COO^- anions (C=O groups: ~1650 cm^{-1}, C–F bond: ~1200 cm^{-1}) and OH groups (>3000 cm^{-1}). According to energy gap law, an increase in the non-radiative decay rate is assisted by the decreasing number of phonons needed to cover the energy gap, ΔE. Since OH groups are characterized by higher vibrational energy than CF_3COO^- anions, we assumed that OH groups with higher phonon energies play a major role in non-radiative relaxation from the $^5D_4$ state. In this way, a maximum of five OH phonons are needed to cover the $^5D_4 \rightarrow {}^7F_0$ energy gap of Tb^{3+} ions (ΔE = 15,000 cm^{-1}); therefore, the probability of non-radiative depopulation from the $^5D_4$ state in xerogels is relatively high.

A comparison of luminescence lifetimes of the $^5D_4$ state for xerogels singly doped with Tb^{3+} ions and co-doped with Tb^{3+}/Eu^{3+} ions reveals a slight shortening when Tb^{3+} ions coexist with Eu^{3+} ions in the same host. Indeed, it was reported that there was a decrease from 0.97 ± 0.01 to 0.82 ± 0.03 ms for XG-Y/Tb^{3+},Eu^{3+} and from 0.89 ± 0.02 to 0.75 ± 0.03 ms for XG-La/Tb^{3+},Eu^3. Therefore, such an effect is a clear evidence of $Tb^{3+} \rightarrow Eu^{3+}$ energy transfer occurrence. The energy transfer efficiency (η_{ET}) between Tb^{3+} and Eu^{3+} ions could be expressed by the following Equation [54,58]:

$$\eta_{ET} = \left(1 - \frac{\tau}{\tau_0}\right) \times 100\% \quad (2)$$

where τ and τ_0 correspond to intrinsic the decay lifetime of the $^5D_4$ excited level of Tb^{3+} in the presence and absence of acceptor ions (Eu^{3+}) in the host lattice, respectively. Indeed, the shortening of the donor's lifetime when the acceptor coexists is a measure of its ability for energy transfer. The energy transfer efficiencies for prepared xerogels are depicted in Table 1. The calculated efficiencies of $Tb^{3+} \rightarrow Eu^{3+}$ energy transfer for both of co-doped xerogels are comparable and they are close to $\eta_{ET} \approx 16\%$. The comparability in η_{ET} values is a consequence of the chemical similarity of the nearest framework around rare-earths (Tb^{3+}, Eu^{3+}) in xerogels. Such relatively low efficiencies are correlated with the long interionic distances between Tb^{3+} and Eu^{3+} ions dispersed within silicate sol-gel host.

Table 1. Luminescence lifetimes of the $^5D_4$ state of Tb^{3+} (τ) and ET efficiencies (η_{ET}) for fabricated silicate xerogels.

Sample	$\tau(^5D_4)$ (ms)	η_{ET} (%)
XG-Y/Tb^{3+},Eu^{3+}	0.82 ± 0.03	15.5
XG-Y/Tb^{3+}	0.97 ± 0.01	-
XG-La/Tb^{3+},Eu^{3+}	0.75 ± 0.03	15.7
XG-La/Tb^{3+}	0.89 ± 0.02	-

For glass-ceramic samples the recorded decay curves are well-fitted to double-exponential functions, which can be expressed by following Equation:

$$I(t)/I_0 = A_1 \times \exp(-t/\tau_1) + A_2 \times \exp(-t/\tau_2), \quad (3)$$

where τ_1 is the decay time of a short lifetime component, τ_2 is the decay time of a long component, while the A_1 and A_2 parameters are amplitudes at t = 0. The double-exponential character of the decay curves clearly means that Tb^{3+} ions are distributed between two different surroundings in which decay processes take place with variable rates. The first of them is a silicate sol-gel network in which the luminescence lifetimes of the $^5D_4$ state of Tb^{3+} ions are shorter (τ_1 decay component) due to presence of high-vibrational energy modes in their local framework (numerous Q^3 units of SiO_4 tetrahedrons (~1050 cm^{-1}) and residual Si–OH groups (>3000 cm^{-1})). The second surrounding is according to fluorides, i.e., YF_3 and LaF_3 nanocrystals. Due to their low-phonon energies close to ~358 (YF_3 phase) and ~350 cm^{-1} (LaF_3 phase), the radiative relaxation from the $^5D_4$ excited state is strongly promoted, and thus, the luminescence lifetimes are considerably prolonged (τ_2 decay component). In other words,

the change in decay profiles from mono-exponential functions (for xerogels) into double-exponential functions (for GCs) is evident proof, which allowed us to conclude that dopant ions are located either in a silicate sol-gel host or fluoride nanocrystals.

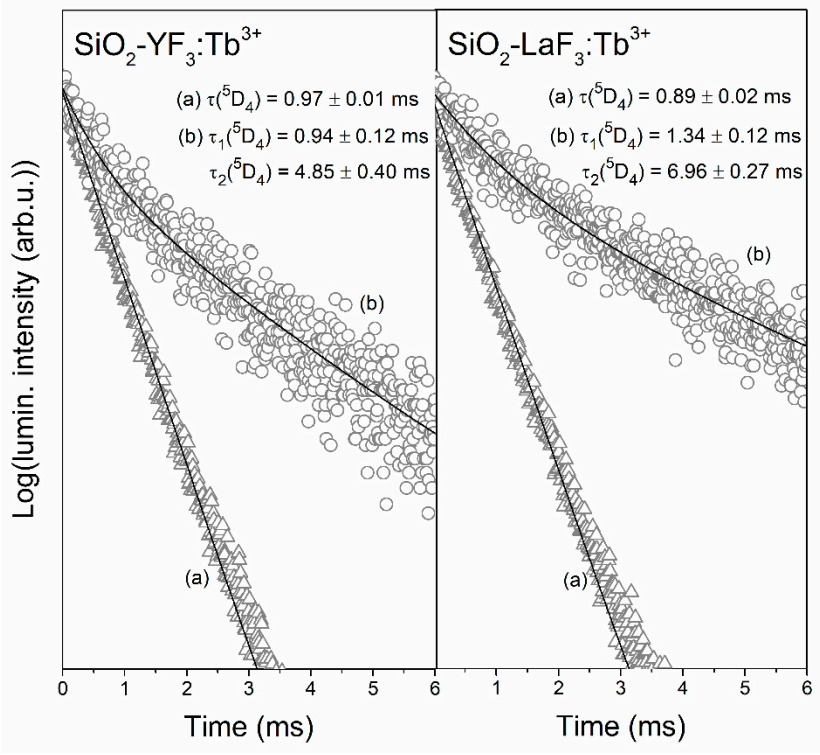

Figure 9. Luminescence decay curves of the $^5D_4$ state of Tb^{3+} recorded for xerogels (**a**) and glass-ceramics (**b**) singly doped with Tb^{3+} ions.

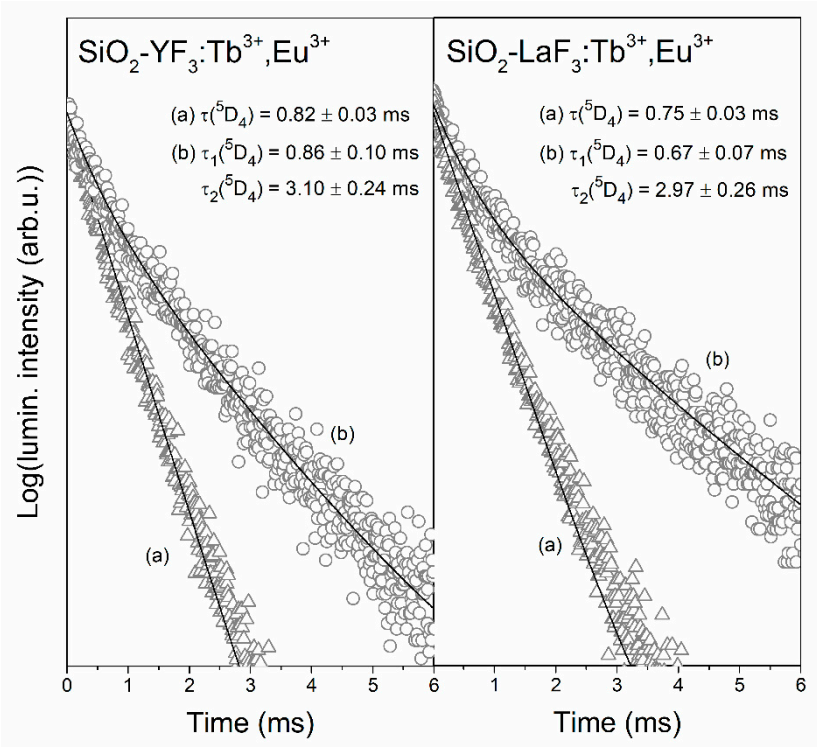

Figure 10. Luminescence decay curves of the $^5D_4$ state of Tb^{3+} recorded for xerogels (**a**) and glass-ceramics (**b**) co-doped with Tb^{3+}/Eu^{3+} ions.

It is quite interesting that the $\tau_2(^5D_4)$ component for SiO_2-LaF_3:Tb^{3+} GC is longer (6.96 ± 0.27 ms) compared with the $\tau_2(^5D_4)$ component for SiO_2-YF_3:Tb^{3+} GC (4.85 ± 0.40 ms). Since the phonon energies of YF_3 and LaF_3 fluoride phases are almost the same, we assumed that such difference in τ_2 lifetime values may suggest that the migration of Tb^{3+} ions from silicate sol-gel host into LaF_3 phase could be more efficient than into YF_3 nanocrystals. It should be also pointed out that co-doping with Eu^{3+} ions lead to the considerable shortening of $\tau_2(^5D_4)$ components due to occurrence of $Tb^{3+} \rightarrow Eu^{3+}$ ET process (3.10 ± 0.24 ms for SiO_2-YF_3:Tb^{3+},Eu^{3+} GC and 2.97 ± 0.26 ms for SiO_2-LaF_3:Tb^{3+},Eu^{3+} GC). To estimate the energy transfer efficiencies, we used the average luminescence lifetimes of the $^5D_4$ state for glass-ceramic materials singly doped with Tb^{3+} and co-doped with Tb^{3+}/Eu^{3+} ions calculated from the following Equation [59]:

$$\tau_{avg} = \frac{A_1\tau_1^2 + A_2\tau_2^2}{A_1\tau_1 + A_2\tau_2} \quad (4)$$

where A_1 and A_2 are fitting constants, and τ_1 and τ_2 are short and long decay components, respectively.

To determine the percentage contribution of short- (τ_1) and long-lived (τ_2) components involved in the total decay process, the following equations were used:

$$\%, \tau_1 = \frac{A_1}{A_1 + A_2} \times 100\%, \quad (5)$$

$$\%, \tau_2 = \frac{A_2}{A_1 + A_2} \times 100\%. \quad (6)$$

For both SiO_2-YF_3:Tb^{3+} as well as SiO_2-YF_3:Tb^{3+},Eu^{3+} GCs, the percentage contributions of τ_1 and τ_2 are quite comparable and equal nearly 50%. A slightly different observation was attained for GCs containing LaF_3 nanocrystals. The difference in contribution of τ_1 and τ_2 decay components is slightly more visible for GCs containing LaF_3 nanocrystals. For the sample singly doped with Tb^{3+} ions, the contribution of the τ_2 component is slightly larger (56.42%) than that of the τ_1 component (43.58%); meanwhile, co-doping with Eu^{3+} ions results in an increase in the τ_1 component's contribution (57.16%) and slight decrease in τ_2 contribution (42.84%). The luminescence lifetimes of the $^5D_4$ state of Tb^{3+} ions, their percentage contribution (%, $\tau_n(^5D_4)$), average lifetimes (τ_{avg}) and the $Tb^{3+} \rightarrow Eu^{3+}$ ET efficiencies (η_{ET}) for fabricated GCs are depicted in Table 2.

Table 2. Luminescence lifetimes of the $^5D_4$ state of Tb^{3+}, their contribution and energy transfer (ET) efficiencies (η_{ET}) for fabricated glass-ceramics.

Sample	$\tau(^5D_4)$ (ms)	%,$\tau_n(^5D_4)$	$\tau_{avg}(^5D_4)$ (ms)	η_{ET} (%)
SiO_2-YF_3:Tb^{3+},Eu^{3+}	0.86 ± 0.10 (τ_1) 3.10 ± 0.24 (τ_2)	49.79% (τ_1) 50.21% (τ_2)	2.62	37.3
SiO_2-YF_3:Tb^{3+}	0.94 ± 0.12 (τ_1) 4.85 ± 0.40 (τ_2)	51.50% (τ_1) 48.50% (τ_2)	4.18	-
SiO_2-LaF_3:Tb^{3+},Eu^{3+}	0.67 ± 0.07 (τ_1) 2.97 ± 0.26 (τ_2)	57.16% (τ_1) 42.84% (τ_2)	2.44	60.8
SiO_2-LaF_3:Tb^{3+}	1.34 ± 0.12 (τ_1) 6.96 ± 0.27 (τ_2)	43.58% (τ_1) 56.42% (τ_2)	6.23	-

It was observed that the average luminescence lifetime for SiO_2-LaF_3:Tb^{3+},Eu^{3+} GC ($\tau_{avg}(^5D_4)$ = 2.44 ms) is 2.6-fold shorter than for SiO_2-LaF_3:Tb^{3+} GC ($\tau_{avg}(^5D_4)$ = 6.23 ms), while for SiO_2-YF_3:Tb^{3+},Eu^{3+} GC ($\tau_{avg}(^5D_4)$ = 2.62 ms), it is 1.6-fold shorter than for SiO_2-YF_3:Tb^{3+} GC ($\tau_{avg}(^5D_4)$ = 4.18 ms). The greater shortening of $\tau_{avg}(^5D_4)$ luminescence lifetime for SiO_2-LaF_3:Tb^{3+},Eu^{3+} GC than for SiO_2-YF_3:Tb^{3+},Eu^{3+} GC indicates a more efficient $Tb^{3+} \rightarrow Eu^{3+}$ energy transfer. Indeed, the calculated ET efficiency value for SiO_2-LaF_3:Tb^{3+},Eu^{3+} (η_{ET} = 60.8%) is about 1.6-fold higher than for SiO_2-YF_3:Tb^{3+},Eu^{3+} (η_{ET} = 37.3%). It should also be noted that the transformation from xerogels into glass-ceramic materials during controlled heat-treatment strongly determines the $Tb^{3+} \rightarrow Eu^{3+}$

energy transfer efficiency, η_{ET}, which increased from ~16% (xerogels) up to 37.3% (SiO_2-YF_3:Tb^{3+},Eu^{3+} GCs) and 60.8% (SiO_2-LaF_3:Tb^{3+},Eu^{3+} GCs).

The luminescence decay curves of the $^5D_0$ state of Eu^{3+} ions in xerogels and SiO_2-YF_3:Tb^{3+},Eu^{3+} as well as SiO_2-LaF_3: Tb^{3+},Eu^{3+} glass-ceramics were recorded for λ_{em} = 611 nm (Figure 11). Similarly, as in the case of decay curves recorded for the $^5D_4$ state of Tb^{3+} ions, the curves of the $^5D_0$ level are well-fitted to mono-exponential functions for xerogels and to double-exponential functions for GCs. Relatively short luminescence lifetimes for xerogels are caused by the coordination of Eu^{3+} ions by high-vibrational OH groups, which are involved in the non-radiative depopulation of the $^5D_0$ level (only four phonons are needed to cover energy gap, ΔE = 12,500 cm^{-1}). Since controlled heat-treatment of xerogels resulted in the partial migration of Eu^{3+} ions inside fluoride nanocrystals, we distinguished two significantly different luminescence lifetimes (τ_1, τ_2). From the decays, it could be concluded that there is a clear correlation between the designated luminescence lifetimes and energy transfer efficiencies (η_{ET}) related to the relative distribution of rare-earths between silicate sol-gel host and fluoride environment. The higher energy transfer efficiency for SiO_2-LaF_3:Tb^{3+},Eu^{3+} (η_{ET} = 60.8%) results in longer decay components ($\tau_1(^5D_0)$ = 0.74 ± 0.04 ms, $\tau_2(^5D_0)$ = 6.84 ± 0.29 ms) than for SiO_2-YF_3:Tb^{3+},Eu^{3+} ($\tau_1(^5D_0)$ = 0.83 ± 0.08 ms, $\tau_2(^5D_0)$ = 5.67 ± 0.39 ms) with lower $Tb^{3+} \rightarrow Eu^{3+}$ energy transfer efficiency (η_{ET} = 37.3%). Indeed, it was observed that the average luminescence lifetime for SiO_2-LaF_3:Tb^{3+},Eu^{3+} ($\tau_{avg}(^5D_0)$ = 5.87 ms) is longer than the average lifetime for SiO_2-YF_3:Tb^{3+},Eu^{3+} ($\tau_{avg}(^5D_0)$ = 4.59 ms). Such an effect could also indicate that the interionic distance between neighboring Tb^{3+} and Eu^{3+} ions in LaF_3 nanocrystals seems to be shorter than in the YF_3 crystal lattice. In other words, this could suggest that the segregation of rare-earths inside the LaF_3 crystal phase is greater, which promotes the $Tb^{3+} \rightarrow Eu^{3+}$ ET. The luminescence decay times, their percentage distribution as well as average lifetimes for both types of fabricated GC sample are depicted in Table 3.

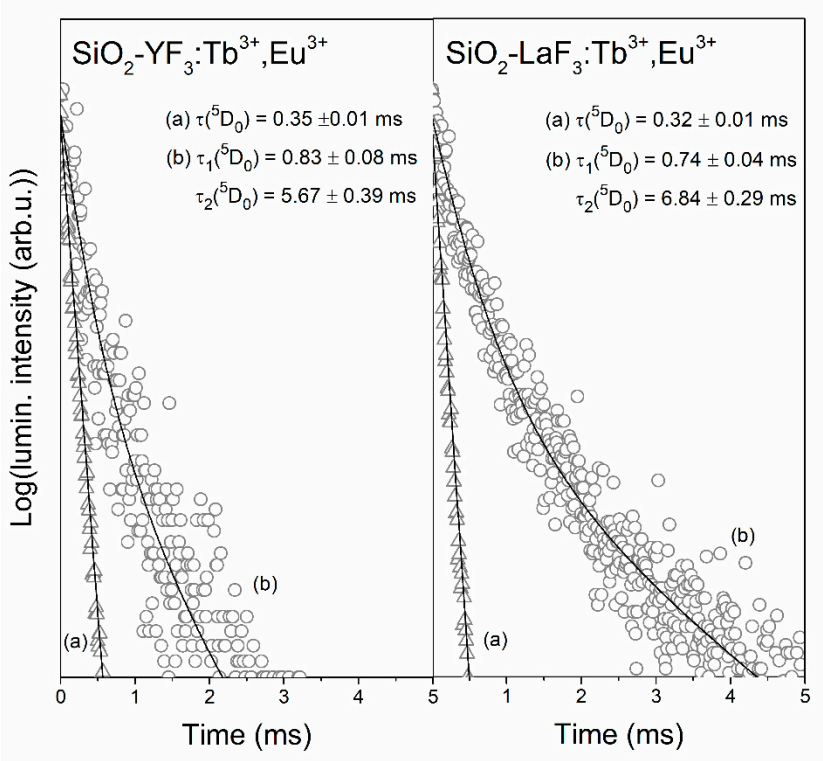

Figure 11. Luminescence decay curves of the $^5D_0$ state of Eu^{3+} recorded for xerogels (**a**) and glass-ceramics (**b**) co-doped with Tb^{3+}/Eu^{3+} ions.

Table 3. Luminescence lifetimes of the $^5D_0$ state of Eu^{3+} and their contributions for fabricated glass-ceramics.

Sample	$\tau(^5D_0)$ (ms)	%, $\tau_n(^5D_0)$	$\tau_{avg}(^5D_0)$ (ms)
SiO_2-YF_3:Tb^{3+},Eu^{3+}	0.83 ± 0.08 (τ_1) 5.67 ± 0.39 (τ_2)	66.30% (τ_1) 33.70% (τ_2)	4.59
SiO_2-LaF_3:Tb^{3+},Eu^{3+}	0.74 ± 0.04 (τ_1) 6.84 ± 0.29 (τ_2)	63.58% (τ_1) 36.42% (τ_2)	5.87

The optical characterization of fabricated co-doped sol-gel samples was supplemented with calculations of quantum yields, ϕ_{Eu}. The quantum efficiencies were calculated from $\phi = k_R/k$ formula in which k is the total decay rate constant ($k = 1/\tau$) and k_R is the radiative rate constant estimated from the following Equation [60]:

$$k_R = A_{MD,0} n^3 \left(\frac{I_{tot}}{I_{MD}} \right). \quad (7)$$

In above equation, $A_{MD,0}$ is according to the Einstein spontaneous emission coefficient for the $^5D_0 \rightarrow {}^7F_1$ transition (14.65 s^{-1} [61]); I_{tot} is the sum of integrated intensities of the $^5D_0 \rightarrow {}^7F_J$ (J = 0–4) luminescence bands of Eu^{3+}; I_{MD} is the integrated intensity of the $^5D_0 \rightarrow {}^7F_1$ magnetic-dipole transition and n is the refractive index. The refractive index of YF_3 and LaF_3 nanocrystals is almost the same and equals n = 1.55–1.56. Such values are comparable with previously published results [62,63]. It is quite interesting that the refractive index of LaF_3 nanocrystals is slightly lower than that of the corresponding LaF_3 single crystal, as was proven by Z. Wang et al. [64]. Finally, the calculated quantum yields are depicted in Table 4.

Table 4. Quantum yields (ϕ_{Eu}) calculated for fabricated xerogels and glass-ceramic materials.

Sample	ϕ_{Eu} (%)
XG-Y/Tb^{3+},Eu^{3+}	9.2
XG-La/Tb^{3+},Eu^{3+}	8.1
SiO_2-YF_3:Tb^{3+},Eu^{3+}	73.0
SiO_2-LaF_3:Tb^{3+},Eu^{3+}	49.5

The quantum efficiencies for xerogels are comparable and equal to 9.2% for XG-Y/Tb^{3+},Eu^{3+} and 8.1% for XG-La/Tb^{3+},Eu^{3+}. Much greater differences in quantum efficiencies were denoted for fabricated glass-ceramics. In fact, the ϕ_{Eu} calculated for SiO_2-YF_3:Tb^{3+},Eu^{3+} GC equal to 49.5%, meanwhile for SiO_2-LaF_3:Tb^{3+},Eu^{3+} GC sample, the ϕ_{Eu} value achieve even 73.0%. The observed significant difference is clearly related to $Tb^{3+} \rightarrow Eu^{3+}$ energy transfer, the efficiency of which is much greater for SiO_2-LaF_3:Tb^{3+},Eu^{3+} (η_{ET} = 60.8%) compared with SiO_2-YF_3:Tb^{3+},Eu^{3+} glass-ceramics (η_{ET} = 37.3%). Based on the current literature, the luminescence quantum yields for Tb^{3+},Eu^{3+} co-doped nanocrystals are usually in a range from 32% to 61% [65]. It is very interesting that the ϕ_{Eu} value for SiO_2-YF_3:Tb^{3+},Eu^{3+} is in good accordance with the presented data, but the SiO_2-LaF_3:Tb^{3+},Eu^{3+} GC sample is characterized by a greater quantum efficiency value. Furthermore, as was proven by N. Shrivastava et al. [66], the quantum yields for LaF_3:Eu^{3+} nanocrystals could vary from 67% up to 85% depending on the Eu^{3+} concentration. Therefore, the obtained results suggest that fabricated sol-gel glass-ceramics could be considered as quite good candidates for visible light-emitting devices.

4. Conclusions

In this work, SiO_2-MF_3:Tb^{3+},Eu^{3+} (M = Y, La) glass-ceramic materials were prepared via sol-gel method during the controlled heat-treatment of silicate xerogels at 350 °C. The performed systematic photoluminescence measurements confirmed that fabricated sol-gel materials exhibit multicolor emission due to the coexistence of the characteristic emission bands originating from both dopant

ions, i.e., Tb^{3+} ($^5D_4 \rightarrow {}^7F_J$, J = 6–3) and Eu^{3+} ($^5D_0 \rightarrow {}^7F_J$, J = 0–4) due to $Tb^{3+} \rightarrow Eu^{3+}$ energy transfer occurrence. Based on performed luminescence decay analysis from the $^5D_4$ (Tb^{3+}) and the $^5D_0$ (Eu^{3+}) excited levels, the correlation between luminescence lifetimes and the distribution of rare-earth ions between the silicate sol-gel host and fluoride nanocrystals was clearly proven. Hence, it was suggested that more preferable segregation of rare-earth ions inside LaF_3 nanocrystals occurred. Moreover, the transformation from xerogels into glass-ceramic materials during controlled heat-treatment determines the strong influence on $Tb^{3+} \rightarrow Eu^{3+}$ energy transfer efficiency, η_{ET}, which increased from ~16% (xerogels) up to 37.3% and 60.8% (SiO_2-YF_3:Tb^{3+},Eu^{3+} and SiO_2-LaF_3:Tb^{3+},Eu^{3+} glass-ceramics, respectively). The obtained luminescent results clearly suggest that the prepared sol-gel glass-ceramic materials could be considered as promising candidates for use as optical elements in RGB-lighting optoelectronic devices operating under NUV excitation.

Author Contributions: Conceptualization, N.P., B.S.-S. and W.A.P.; methodology, N.P., B.S.-S. and W.A.P.; software, N.P.; validation, N.P. and W.A.P.; formal analysis, W.A.P.; investigation, N.P.; resources, N.P. and W.A.P.; data curation, N.P.; writing—original draft preparation, N.P.; writing—review and editing, W.A.P.; visualization, N.P.; supervision, N.P. and W.A.P.; project administration, W.A.P.; funding acquisition, W.A.P. All authors have read and agreed to the published version of the manuscript.

Funding: This research was funded by National Science Centre (Poland), grant number 2016/23/B/ST8/01965.

Conflicts of Interest: The authors declare no conflict of interest.

References

1. Jamalaiah, B.C.; Venkatramaiah, N.; Rao, T.R.; Rasool, S.N.; Rao, B.N.; Ram, D.V.R.; Reddy, A.S.N. UV excited $SrAl_2O_4$: Tb^{3+} nanophosphors for photonic applications. *Mat. Sci. Semicon. Proc.* **2020**, *105*, 104722. [CrossRef]
2. Dalmis, R.; Keskin, O.Y.; Azem, N.F.A.; Birlik, I. A new one-dimensional photonic crystal combination of TiO_2/CuO for structural color applications. *Ceram. Int.* **2019**, *45*, 21333–21340. [CrossRef]
3. Bian, W.; Lin, Y.; Wang, T.; Yu, X.; Qiu, J.; Zhou, M.; Luo, H.; Yu, S.F.; Xu, X. Direct Identification of surface defects and their influence on the optical characteristics of upconversion nanoparticles. *ACS Nano* **2018**, *12*, 3623–3628. [CrossRef] [PubMed]
4. Gong, G.; Song, Y.; Tan, H.; Xie, S.; Zhang, C.; Xu, L.; Xu, J.; Zheng, J. Design of core/active-shell $NaYF_4$:Ln^{3+}@$NaYF_4$:Yb^{3+} nanophosphors with enhanced red-green-blue upconversion luminescence for anti-counterfeiting printing. *Compos. Part B—Eng.* **2019**, *179*, 107504. [CrossRef]
5. Wang, T.; Yu, H.; Siu, C.K.; Qiu, J.; Xu, X.; Yu, S.F. White-light whispering-gallery-mode lasing from lanthanide-doped upconversion $NaYF_4$ hexagonal microrods. *ACS Photonics* **2017**, *4*, 1539–1543. [CrossRef]
6. Chen, J.; Peng, Y.; Li, X.; Chen, W.; Huang, H.; Lin, L.; Chen, D. Near-infrared-laser-driven robust glass-ceramic-based upconverted solid-state lighting. *J. Mater. Chem. C* **2019**, *7*, 4109–4117. [CrossRef]
7. Li, Z.; Zhou, D.; Yang, Y.; Ren, P.; Qiu, J. Adjustable multicolor up-energy conversion in light-luminescence in Tb^{3+}/Tm^{3+}/Yb^{3+} co-doped oxyfluoride glass-ceramics containing Ba_2LaF_7 nanocrystals. *Sci. Rep.* **2017**, *7*, 6518. [CrossRef]
8. do Carmo, F.F.; do Nascimento, J.P.C.; Façanha, M.X.; Sales, T.O.; Santos, W.Q.; Gouveia-Neto, A.S.; Jacinto, C.; Sombra, A.B.S. White light upconversion emission and color tunability in Er^{3+}/Tm^{3+}/Yb^{3+} tri-doped $YNbO_4$ phosphor. *J. Lumin.* **2018**, *204*, 676–684. [CrossRef]
9. Li, M.; Wang, L.; Ran, W.; Deng, Z.; Ren, C.; Shi, J. Tunable emission of single-phased $NaY(WO_4)_2$: Sm^{3+} phosphor based on energy transfer. *Ceram. Int.* **2017**, *43*, 6751–6757. [CrossRef]
10. Li, Z.; Zhong, B.; Cao, Y.; Zhang, S.; Lv, Y.; Mu, Z.; Hu, Z.; Hu, Y. Energy transfer and tunable luminescence properties in $Y_3Al_2Ga_3O_{12}$:Tb^{3+},Eu^{3+} phosphors. *J. Alloy. Compd.* **2019**, *787*, 672–682. [CrossRef]
11. Liu, Y.; Liu, G.; Wang, J.; Dong, X.; Yu, W. Single-component and warm-white-emitting phosphor $nagd(wo_4)_2$:Tm^{3+},Dy^{3+},Eu^{3+}: Synthesis, luminescence, energy transfer, and tunable color. *Inorg. Chem.* **2014**, *53*, 11457–11466. [CrossRef] [PubMed]
12. Lü, Y.; Tang, X.; Yan, L.; Li, K.; Liu, X.; Shang, M.; Li, C.; Lin, J. Synthesis and luminescent properties of $GdNdO_4$:RE^{3+} (RE = Tm, Dy) nanocrystalline phosphors via the sol-gel process. *J. Phys. Chem. C* **2013**, *117*, 21972–21980. [CrossRef]

13. Baur, F.; Glocker, F.; Jüstel, T. Photoluminescence and energy transfer rates and efficiencies in Eu^{3+} activated $Tb_2Mo_3O_{12}$. *J. Mater. Chem. C* **2015**, *3*, 2054–2064. [CrossRef]
14. Xu, M.; Ding, Y.; Luo, W.; Wang, L.; Li, S.; Liu, Y. Synthesis, luminescence properties and energy transfer behavior of color-tunable $KAlP_2O_7$:Tb^{3+},Eu^{3+} phosphors. *Opt. Laser Technol.* **2020**, *121*, 105829. [CrossRef]
15. Chen, Z.; Chen, X.; Huang, S.; Pan, Y. A novel tunable green-to-red emitting phosphor $Ca_4LaO(BO_3)_3$:Tb,Eu via energy transfer with high quantum yield. *Ceram. Int.* **2016**, *42*, 13476–13484. [CrossRef]
16. Kukku, T.; Dinu, A.; Sisira, S.; Gopi, S.; Biju, P.R.; Unnikrishnan, N.V.; Cryriac, J. Energy transfer driven tunable emission of Tb/Eu co-doped lanthanum molybdates nanophosphors. *Opt. Mater.* **2018**, *80*, 37–46.
17. dos, S.; Bezerra, C.; Valerio, M.E.G. Structural and optical study of CaF_2 nanoparticles produced by a microwave-assisted hydrothermal method. *Phys. B Condens. Matter* **2016**, *501*, 106–112.
18. Rivera-López, F.; Babu, P.; Basavapoornima, C.; Jayasankar, C.K.; Lavín, V. Efficient $Nd^{3+} \rightarrow Yb^{3+}$ energy transfer processes in high phonon energy phosphate glasses for 1.0 μm Yb^{3+} ions. *J. Appl. Phys.* **2011**, *109*, 123514. [CrossRef]
19. Cao, R.; Lu, Y.; Tian, Y.; Huang, F.; Xu, S.; Zhang, J. Spectroscopy of thulium and holmium co-doped silicate glasses. *Opt. Mater. Express* **2016**, *6*, 2252–2263. [CrossRef]
20. Suo, H.; Guo, C.; Zheng, J.; Zhou, B.; Ma, C.; Zhao, X.; Li, T.; Guo, P.; Goldys, E.M. Sensitivity modulation of upconverting thermometry through engineering phonon energy of a matrix. *ACS Appl. Mater. Interfaces* **2016**, *8*, 32312–32319. [CrossRef]
21. Biswas, A.; Maciel, G.S.; Friend, C.S.; Prasad, P.N. Upconversion properties of a transparent Er^{3+}-Yb^{3+} co-doped LaF_3-SiO_2 glass-ceramics prepared by sol-gel method. *J. Non-Cryst. Solids* **2003**, *316*, 393–397. [CrossRef]
22. Jacobsohn, L.G.; McPherson, C.L.; Oliveira, L.C.; Kucera, C.J.; Ballato, J.; Yukihara, E.G. Radioluminescence and thermoluminescence of rare earth doped and co-doped YF_3. *Radiat. Meas.* **2017**, *106*, 79–83. [CrossRef]
23. Milovanov, Y.S.; Skryshevsky, V.A.; Tolstoy, V.P.; Gulina, L.B.; Gavrilchenko, I.V.; Kuznetsov, G.V. Photoluminescence of porous silicon coated by SILD method with LaF_3 nanolayers. *Curr. Appl. Phys.* **2013**, *13*, 1625–1629. [CrossRef]
24. Du, Y.; Han, S.; Zou, Y.; Yuan, J.; Shao, C.; Jiang, X.; Chen, D. Luminescence properties of Ce^{3+}-doped oxyfluoride aluminosilicate glass and glass ceramics. *Opt. Mater.* **2019**, *89*, 243–249. [CrossRef]
25. Montoya-Quesada, E.; Villaquirán-Caicedo, M.A.; Mejía de Gutiérrez, R.; Muñoz-Saldaña, J. Effect of ZnO content on the physical, mechanical and chemical properties of glass-ceramics in the CaO-SiO_2-Al_2O_3 system. *Ceram. Int.* **2020**, *46*, 4322–4328. [CrossRef]
26. Wang, T.; Wang, S.; Wei, Y.; Zhou, X.; Zhang, H.; Wang, L.; Guo, Z.; Lv, H. Preparation and luminescence properties of Eu_2O_3 doped glass-ceramics containing $NaY(MoO_4)_2$. *J. Eur. Ceram. Soc.* **2020**, *40*, 1671–1676. [CrossRef]
27. Marcondes, L.M.; Evangelista, R.O.; Gonçalves, R.R.; de Camargo, A.S.S.; Manzani, D.; Nalin, M.; Cassanjes, F.C.; Poirier, G.Y. Er^{3+}-doped niobium alkali germanate glasses and glass-ceramics: NIR and visible luminescence properties. *J. Non-Cryst. Solids* **2019**, *521*, 119492. [CrossRef]
28. Cheng, C.; Zeng, N.; Jiao, Q.; Zhang, X.; Liu, X. Tunable upconversion white photoemission in Yb^{3+}/Mn^{2+}/Tm^{3+} tri-doped transparent glass ceramics. *Opt. Mater.* **2020**, *100*, 109718. [CrossRef]
29. Fedorov, P.P.; Luginina, A.A.; Popov, A.I. Transparent oxyfluoride glass ceramics. *J. Fluor. Chem.* **2015**, *172*, 22–50. [CrossRef]
30. Yu, H.; Guo, H.; Zhang, M.; Liu, Y.; Liu, M.; Zhao, L. Distribution of Nd^{3+} ions in oxyfluoride glass ceramics. *Nanoscale Res. Lett.* **2012**, *7*, 275. [CrossRef]
31. del-Castillo, J.; Yanes, A.C.; Méndez-Ramos, J.; Tikhomirov, V.K.; Moshchalkov, V.V.; Rodríguez, V.D. Sol-gel preparation and white up-conversion luminescence in rare-earth doped PbF_2 nanocrystals dissolved in silica glass. *J. Solgel Sci. Technol.* **2010**, *53*, 509–514. [CrossRef]
32. Leśniak, M.; Żmojda, J.; Kochanowicz, M.; Miluski, P.; Baranowska, A.; Mach, G.; Kuwik, M.; Pisarska, J.; Pisarski, W.A.; Dorosz, D. Spectroscopic properties of erbium-doped oxyfluoride phospho-tellurite glass and transparent glass-ceramic containing BaF_2 nanocrystals. *Materials* **2019**, *12*, 3429. [CrossRef]
33. Lisiecki, R.; Ryba-Romanowski, W. Silica-based oxyfluoride glass and glass-ceramic doped with Tm^{3+} and Yb^{3+}-VUV-VIS-NIR spectroscopy and optical thermometry. *J. Alloys Compd.* **2020**, *814*, 152304. [CrossRef]
34. Hu, Z.; Wang, Y.; Bao, F.; Luo, W. Crystallization behavior and microstructure investigations on LaF_3 containing oxyfluoride glass ceramics. *J. Non-Cryst. Solids* **2005**, *351*, 722–728. [CrossRef]

35. Zhang, Z.; Li, K.; Liu, C.; Yin, Q.; Han, J.; Heo, J. Intense up-conversion emission from Er^{3+}/Yb^{3+} ion co-doped transparent oxyfluoride glass-ceramics containing $Y_5O_4F_7$ nanorods for optical thermometry. *J. Mater. Chem. C* **2019**, *7*, 6134–6143.
36. Zhang, X.; Hu, L.; Ren, J. Transparent aluminosilicate oxyfluoride glass ceramics containing upconversion luminescent caf_2 nanocrystals: Glass-to-crystal structural evolution studied by the advanced solid-state nmr spectroscopy. *J. Mater. Chem. C* **2020**, *124*, 1594–1608. [CrossRef]
37. Antuzevics, A.; Kemere, M.; Krieke, G.; Ignatans, R. Electron paramagnetic resonance and photoluminescence investigation of europium local structure in oxyfluoride glass ceramics containing SrF_2 nanocrystals. *Opt. Mater.* **2017**, *72*, 749–755. [CrossRef]
38. Zhou, B.; E, C.Q.; Bu, Y.Y.; Meng, L.; Yan, X.H.; Wang, X.F. Temperature-controlled down-conversion luminescence behavior of Eu^{3+}-doped transparent MF_2 (M = Ba, Ca, Sr) glass ceramics. *Luminescence* **2017**, *32*, 195–200. [CrossRef]
39. Biswas, K.; Sontakke, A.D.; Sen, R.; Annapurna, K. Luminescence properties of dual valence Eu doped nano-crystalline BaF_2 embedded glass-ceramics and observation of $Eu^{2+} \rightarrow Eu^{3+}$ energy transfer. *J. Fluoresc.* **2012**, *22*, 745–752. [CrossRef]
40. Gorni, G.; Velázquez, J.J.; Mosa, J.; Balda, R.; Fernández, J.; Durán, A.; Castro, Y. Transparent glass-ceramics produced by sol-gel: A suitable alternative for photonic materials. *Materials* **2018**, *11*, 212. [CrossRef]
41. Velázquez, J.J.; Mosa, J.; Gorni, G.; Balda, R.; Fernández, J.; Durán, A.; Castro, Y. Novel sol-gel SiO_2-$NaGdF_4$ transparent nano-glass-ceramics. *J. Non-Cryst. Solids* **2019**, *520*, 119447. [CrossRef]
42. Gorni, G.; Velázquez, J.J.; Mosa, J.; Mather, G.C.; Serrano, A.; Vila, M.; Castro, G.R.; Bravo, D.; Balda, R.; Fernández, J.; et al. Transparent sol-gel oxyfluoride glass-ceramics with high crystalline fraction and study of re incorporation. *Nanomaterials* **2019**, *9*, 530. [CrossRef]
43. Vinogradov, A.V.; Vinogradov, V.V. Low-temperature sol-gel synthesis of crystalline materials. *RSC Adv.* **2014**, *4*, 45903–45919. [CrossRef]
44. Pawlik, N.; Szpikowska-Sroka, B.; Goryczka, T.; Pisarski, W.A. Photoluminescence investigation of sol-gel glass-ceramic materials containing SrF_2:Eu^{3+} nanocrystals. *J. Alloys Compd.* **2019**, *810*, 151935. [CrossRef]
45. Chen, D.; Wang, Z.; Zhou, Y.; Huang, P.; Ji, Z. Tb^{3+}/Eu^{3+}:YF_3 nanophase embedded glass ceramics: Structural characterization, tunable luminescence and temperature sensing behavior. *J. Alloys Compd.* **2015**, *646*, 339–344. [CrossRef]
46. Pawlik, N.; Szpikowska-Sroka, B.; Goryczka, T.; Zubko, M.; Lelątko, J.; Pisarski, W.A. Structure and luminescent properties of oxyfluoride glass-ceramics with YF_3:Eu^{3+} nanocrystals derived by sol-gel method. *J. Eur. Ceram. Soc.* **2019**, *39*, 5010–5017. [CrossRef]
47. Pawlik, N.; Szpikowska-Sroka, B.; Pietrasik, E.; Goryczka, T.; Pisarski, W.A. Structural and luminescence properties of silica powders and transparent glass-ceramics containing LaF_3:Eu^{3+} nanocrystals. *J. Am. Ceram. Soc.* **2018**, *101*, 4654–4668. [CrossRef]
48. Yanes, A.C.; del-Castillo, J.; Méndez-Ramos, J.; Rodríguez, V.D.; Torres, M.E.; Arbiol, J. Luminescence and structural characterization of transparent nanostructures Eu^{3+}-doped LaF_3-SiO_2 glass-ceramics prepared by sol-gel method. *Opt. Mater.* **2007**, *29*, 999–1003. [CrossRef]
49. Wu, X.; Zheng, J.; Ren, Q.; Zhu, J.; Ren, Y.; Hai, O. Luminescent properties and energy transfer in novel single-phase multicolor tunable $Sr_3Y(BO_3)_3$:Tb^{3+},Eu^{3+} phosphors. *J. Alloys Compd.* **2019**, *805*, 12–18. [CrossRef]
50. Yanes, A.C.; del-Castillo, J.; Ortiz, E. Energy transfer and tunable emission in $BaGdF_5$:RE^{3+} (RE = Ce, Tb, Eu) nano-glass-ceramics. *J. Alloys Compd.* **2019**, *773*, 1099–1107. [CrossRef]
51. Wang, B.; Ren, Q.; Hai, O.; Wu, X. Luminescence properties and energy transfer in Tb^{3+} and Eu^{3+} co-doped $Ba_2P_2O_7$ phosphors. *RSC Adv.* **2017**, *7*, 15222–15227. [CrossRef]
52. Xie, F.; Li, J.; Dong, Z.; Wen, D.; Shi, J.; Yan, J.; Wu, M. Energy transfer and luminescent properties of $Ca_8MgLu(PO_4)_7$:Tb^{3+}/Eu^{3+} as a green-to-red color tunable phosphor under NUV excitation. *RSC Adv.* **2015**, *5*, 59830–59836. [CrossRef]
53. Caldiño, U.; Speghini, A.; Berneschi, S.; Bettinelli, M.; Brenci, M.; Pasquini, E.; Pelli, S.; Righini, G.C. Optical spectroscopy and optical waveguide fabrication in Eu^{3+} and Eu^{3+}/Tb^{3+} doped zinc-sodium-aluminosilicate glasses. *J. Lumin.* **2014**, *147*, 336–340. [CrossRef]

54. Gopi, S.; Jose, S.K.; Sreeja, E.; Manasa, P.; Unnikrishnan, N.V.; Cyriac, J.; Biju, P.R. Tunable green to red emission via Tb sensitized energy transfer in Tb/Eu co-doped alkali fluoroborate glass. *J. Lumin.* **2017**, *192*, 1288–1294. [CrossRef]
55. Liu, H.-G.; Zheng, W.-C. Theoretical investigations of the optical and EPR spectra for trivalent cerium and ytterbium ions in orthorhombic YF_3 crystal. *Phys. B* **2016**, *496*, 15–19. [CrossRef]
56. Rast, H.E.; Caspers, H.H.; Miller, S.A. Infrared Dispersion and Lattice Vibrations of LaF_3. *Phys. Rev.* **1968**, *171*, 1051–1057. [CrossRef]
57. Binnemans, K. Interpretation of europium(III) spectra. *Coord. Chem. Rev.* **2015**, *295*, 1–45. [CrossRef]
58. Li, B.; Huang, X.; Guo, H.; Zeng, Y. Energy transfer and tunable photoluminescence of $LaBWO_6$:Tb^{3+},Eu^{3+} phosphors for near-UV white LEDs. *Dye. Pigment.* **2018**, *150*, 67–72. [CrossRef]
59. Xia, Z.; Zhuang, J.; Liao, L. Novel red-emitting $Ba_2Tb(BO_3)_2Cl$:Eu phosphor with efficient energy transfer for potential application in white light-emitting diodes. *Inorg. Chem.* **2012**, *51*, 7202–7209. [CrossRef]
60. Chen, J.; Meng, Q.; May, P.S.; Berry, M.T.; Lin, C. Sensitization of Eu^{3+} luminescence in Eu:YPO_4 nanocrystals. *J. Phys. Chem. C* **2013**, *117*, 5953–5962. [CrossRef]
61. Werts, M.H.V.; Jukes, R.T.F.; Verhoeven, J.W. The emission spectrum and the radiative lifetime of Eu^{3+} in luminescent lanthanide complexes. *Phys. Chem. Chem. Phys.* **2002**, *4*, 1542–1548. [CrossRef]
62. Zhang, S.-T.; Modreanu, M.; Roussel, H.; Jiménez, C.; Deschanvres, J.-L. Exploring the optical properties of Vernier phase yttrium oxyfluoride thin films grown by pulsed liquid injection MOCVD. *Dalton Trans.* **2018**, *47*, 2655–2661. [CrossRef] [PubMed]
63. Gorni, G.; Balda, R.; Fernández, J.; Velázquez, J.J.; Pascual, L.; Mosa, J.; Durán, A.; Castro, Y. $80SiO_2$-$20LaF_3$ oxyfluoride glass ceramic coatings doped with Nd^{3+} for optical applications. *Int. J. Appl. Glass Sci.* **2018**, *9*, 208–217. [CrossRef]
64. Wang, Z.; Wang, N.; Wang, D.; Tang, Z.; Yu, K.; Wei, W. Method for refractive index measurement of nanoparticles. *Opt. Lett.* **2014**, *39*, 4251–4254. [CrossRef]
65. Lu, P.; Wang, Y.; Huang, L.; Lian, S.; Wang, Y.; Tang, J.; Belfiore, L.A.; Kipper, M.J. Tb^{3+}/Eu^{3+} complex-doped rigid nanoparticles in transparent nanofibrous membranes exhibit high quantum yield fluorescence. *Nanomaterial* **2020**, *10*, 694. [CrossRef]
66. Shrivastava, N.; Khan, L.U.; Vergas, J.M.; Ospina, C.; Coaquira, J.A.Q.; Zoppellaro, G.; Brito, H.F.; Javed, Y.; Shukla, D.K.; Felinto, M.C.F.C.; et al. Efficient multicolor tunability of ultrasmall ternary-doped LaF_3 nanoparticles: Energy conversion and magnetic behavior. *Phys. Chem. Chem. Phys.* **2017**, *19*, 18660–18670. [CrossRef]